Monthly Notices of the ROYAL ASTRONOMICAL SOCIETY
MNRAS **510,** 3321–3334 (2022)
Advance Access publication 2021 November 18
https://doi.org/10.1093/mnras/stab3312

The dust-continuum size of TNG50 galaxies at z = 1–5: a comparison with the distribution of stellar light, stars, dust, and H_2

Gergö Popping [1]★ Annalisa Pillepich [2] Gabriela Calistro Rivera,[1] Sebastian Schulz,[3] Lars Hernquist,[4] Melanie Kaasinen [2,5] Federico Marinacci [6] Dylan Nelson [5,7] and Mark Vogelsberger [8]

[1]European Southern Observatory, Karl-Schwarzschild-Str 2, D-85748 Garching, Germany
[2]Max-Planck-Institut für Astronomie, K'onigstuhl 17, D-69117 Heidelberg, Germany
[3]Institute for Computational Science, University of Zurich, Winterthurerstrasse 190, CH-8057 Zurich, Switzerland
[4]Harvard-Smithsonian Center for Astrophysics, 60 Garden Street, Cambridge, MA 02138, USA
[5]Universität Heidelberg, Zentrum für Astronomie, Institut für Theoretische Astrophysik, Albert-Ueberle-Straße 2, D-69120 Heidelberg, Germany
[6]Department of Physics and Astronomy 'Augusto Righi', University of Bologna, via Gobetti 93/2, I-40129 Bologna, Italy
[7]Max-Planck-Institut fü Astrophysik, Karl-Schwarzschild-Str 1, D-85748 Garching, Germany
[8]Kavli Institute for Astrophysics and Space Research, Department of Physics, MIT, Cambridge, MA 02139, USA

Accepted 2021 November 12. Received 2021 November 12; in original form 2021 January 25

ABSTRACT

We present predictions for the extent of the dust-continuum emission of main-sequence galaxies drawn from the TNG50 simulation in the range z = 1–5. We couple the radiative transfer code SKIRT to the output of the TNG50 simulation and measure the dust-continuum half-light radius of the modelled galaxies, assuming a Milky Way dust type and a metallicity-dependent dust-to-metal ratio. The dust-continuum half-light radius at observed-frame 850 μm is up to ∼75 per cent larger than the stellar half-mass radius, but significantly more compact than the observed-frame 1.6 μm (roughly corresponding to H band) half-light radius, particularly towards high redshifts: the compactness compared to the 1.6 μm emission increases with redshift. This is driven by obscuration of stellar light from the galaxy centres, which increases the apparent extent of 1.6 μm disc sizes relative to that at 850 μm. The difference in relative extents increases with redshift because the observed-frame 1.6 μm emission stems from ever shorter wavelength stellar emission. These results suggest that the compact dust-continuum emission observed in $z > 1$ galaxies is not (necessarily) evidence of the build-up of a dense central stellar component. We find that the dust-continuum half-light radius closely follows the radius containing half the star formation and half the dust mass in galaxies and is ∼80 per cent of the radius containing half the H_2 mass. The presented results are a common feature of main-sequence galaxies.

Key words: radiative transfer – galaxies: evolution – galaxies: ISM – infrared: galaxies – submillimetre: galaxies.

1 INTRODUCTION

In the last decade, the Atacama Large (sub-)Millimeter Array (ALMA) has successfully observed the integrated dust-continuum emission of a few hundred of galaxies at $z > 1$ (and see also Hodge & da Cunha 2020, for a recent review Scoville et al. 2013; Schinnerer et al. 2016). One of the current challenges is to resolve the dust-continuum emission in high-redshift objects. The dust-continuum emission is light from young stars that has been absorbed by dust and re-emitted at infrared (IR) and (sub-)millimeter wavelengths and is often used as a tracer of dust-obscured star formation. Resolved dust-continuum studies will thus provide important information about the location of dust-obscured star formation within galaxies and their link to the stellar build-up of galaxies over cosmic time. In particular, the distribution of dust-continuum emission from main-sequence galaxies [galaxies that lie on the observed correlation between the stellar mass and star formation rate (SFR) that the majority of star-forming galaxies follow, Noeske et al. 2007; Daddi et al. 2008; Whitaker et al. 2014] is still largely unclear.

In recent years, there have been a number of observational studies focusing on the dust-continuum morphology of $z > 1$ galaxies. These studies typically focused on the Far Infrared (FIR) brightest objects (submillimetre galaxies, SMGs, Ikarashi et al. 2015; Simpson et al. 2015; Chen et al. 2017; Gullberg et al. 2019; Hodge et al. 2019). Fujimoto et al. (2017) measured the extent of the dust-continuum emission in a sample of galaxies drawn from the ALMA archive between $z = 0$ and $z = 6$, typically focusing on FIR-bright objects. Nelson et al. (2019c) explored the dust-continuum morphology of a $z = 1.2$ main-sequence galaxy. Rujopakarn et al. (2019) and Kaasinen et al. (2020) resolved the dust-continuum emission of three and two main-sequence galaxies at $z \sim 2.5$ and $z \sim 1.5$, respectively. Barro et al. (2016) used ALMA to resolve the dust-continuum emission of six compact star-forming galaxies at $z \sim 2.5$, whereas Tadaki et al. (2017) studied the dust-continuum distribution in two massive H_α-selected galaxies at $z \sim$ 2.2–2.5. Spilker et al. (2019) probed the extent of the dust continuum emission in a $z \sim 2.2$ compact star-forming galaxy. Recently, Tadaki et al. (2020) explored the 850 μm

★ E-mail: gpopping@eso.org

size of 85 massive ($M_* > 10^{11}\,\mathrm{M}_\odot$) galaxies at $1.9 < z < 2.5$. What all of these observations have in common is that the dust-continuum emission of these galaxies is more compact than their optical or Near-Infrared (NIR) emission. This has been seen as evidence of the dust-obscured build-up of a compact central dense stellar component (e.g. Barro et al. 2016; Tadaki et al. 2020). This conclusion is further supported by the finding that the dust-continuum emission is also more compact than the stellar mass distribution (Calistro Rivera et al. 2018; Lang et al. 2019; Tadaki et al. 2020). Although the aforementioned studies of the resolved dust-continuum emission have been crucial to build our current understanding of obscured star formation in galaxies and the build-up of stellar discs, the number of targets is still mostly limited to $z = 1$–2 main-sequence galaxies, or to very massive galaxies, not representative of the full galaxy population on the main-sequence.

Besides tracing the dust-obscured star formation, the dust-continuum emission of galaxies has also frequently been used as a tracer of the molecular hydrogen (H_2) content of galaxies (e.g. Scoville et al. 2013, 2016; Groves et al. 2015; Schinnerer et al. 2016; Hughes et al. 2017). More detailed studies of individual objects have demonstrated that the H_2 mass of galaxies calculated from their integrated dust-continuum emission is similar to H_2 masses obtained by using the more classical tracer: carbon monooxide (CO) emission lines (Hughes et al. 2017; Popping et al. 2017b; Bertemes et al. 2018; Kaasinen et al. 2019; Aravena et al. 2020). Theoretical efforts have reached similar conclusions (Liang et al. 2018; Privon, Narayanan & Davé 2018). Extended configuration observations with ALMA have allowed a spatial comparison between various tracers of H_2 in galaxies. Observations of the brightest most actively star-forming objects show that the dust-continuum emission is typically more compact than the CO emission (Hodge et al. 2015; Chen et al. 2017; Calistro Rivera et al. 2018). Using resolved observations of two main-sequence galaxies at $z \sim 1.5$, Kaasinen et al. (2020) found that one of the objects has more extended CO emission than dust-continuum emission, whereas in the other the dust-continuum is more extended than the CO (see also Spilker et al. 2019).

It is expected that in the next years the extended baseline capabilities of ALMA will be used to increase the sample size and redshift coverage of main-sequence galaxies with resolved measurements of their dust-continuum emission (as well as CO and other lines). It is thus timely to develop the theoretical framework to yield predictions and put observations in a theoretical context, providing a physical explanation for the observations. In recent years a significant effort went into combining hydrodynamic galaxy-formation simulations with radiative transfer codes such as SUNRISE (Jonsson 2006), SKIRT (Baes et al. 2011; Baes & Camps 2015; Camps & Baes 2015), and Powderday (Narayanan et al. 2020). These tools have allowed theorists to provide direct predictions of the sub-mm dust-continuum emission of model galaxies, to be compared to observations from sub-mm observatories such as ALMA (e.g. Camps et al. 2016; Behrens et al. 2018; Cochrane et al. 2019; Liang et al. 2020; Lovell et al. 2021). The coupling of galaxy formation simulations with such radiative transfer codes is thus an ideal approach towards providing theoretical insights into the dust-continuum morphology of galaxies.

Cochrane et al. (2019) applied radiative transfer calculations with SKIRT on four galaxies modelled with the FIRE-2 simulation (Hopkins et al. 2018), following these galaxies from $z = 5$ to $z = 1$, to study their resolved dust-continuum emission. The authors find that the simulated galaxies have dust-continuum emission that is generally more compact than the cold gas and the dust mass, but more extended than the stellar component. This study marked the first attempt to modelling the dust-continuum morphology of galaxies, but because of its limited sample size, it is hard to draw conclusions about main-sequence galaxies covering a range in galaxy properties (stellar mass, SFR, redshift). One of the reasons is that studies of the resolved simulated properties of galaxies require a high mass resolution (with baryonic mass resolution elements of a few times $10^4\,\mathrm{M}_\odot$ or below) to sufficiently resolve galaxy discs. These simulations are computationally expensive to run for large cosmological volumes probing a wide galaxy parameter space.

The new TNG50 simulation (Nelson et al. 2019b; Pillepich et al. 2019) is the highest resolution variant of the IllustrisTNG simulation suite (Marinacci et al. 2018; Naiman et al. 2018; Nelson et al. 2018; Pillepich et al. 2018b; Springel et al. 2018). With a mass resolution of $M_{\mathrm{baryons}} \sim 8.5 \times 10^4\,\mathrm{M}_\odot$ in a cosmological volume of ~50 cMpc on a side, this simulation is ideal to study a representative sample of galaxies over cosmic time at sufficiently good mass resolution to resolve the inner structure of galaxy discs.

In this work, we couple the TNG50 simulation with the radiative transfer code SKIRT to make predictions for the dust-continuum emission of main-sequence galaxies at $z = 1$–5. This redshift range was chosen to roughly match the observational data (e.g. Hodge et al. 2013; Karim et al. 2013; Fujimoto et al. 2017; Stach et al. 2019; Kaasinen et al. 2020) and to guarantee a decent number of main-sequence galaxies that are sufficiently resolved in the simulation. We specifically aim to address how the dust-continuum size of main-sequence galaxies evolves over cosmic time, if the dust-continuum emission is more compact than the stellar component and the optical/NIR emission of galaxies, and how well the dust-continuum emission of galaxies correlates with the distribution of H_2, dust mass, and star formation in galaxies. We furthermore explore how the size of galaxies changes as a function of sub-mm wavelengths.

The structure of the paper is as follows. In Section 2, we present the methodology by introducing the TNG50 simulation and the SKIRT radiative transfer code, as well as the galaxy selection and our approach to measuring the sizes of the modelled galaxies. In Section 3, we present the predictions by the model and we discuss these in Section 4. A summary and conclusion of the results presented in this work is given in Section 5. Throughout this work, we mostly focus on the 850 μm size of galaxies (although see Section 3.1). The observed-frame emission at 850 μm is covered by ALMA band 7 and is frequently used to study the dust-continuum emission of galaxies (e.g. Hodge et al. 2013; Barro et al. 2016; Chen et al. 2017; Stach et al. 2019; Tadaki et al. 2020).

2 DESCRIPTION OF THE MODEL

2.1 The TNG50 simulation

In this paper, we use the TNG50 simulation (Nelson et al. 2019b; Pillepich et al. 2019). This simulation is part of the IllustrisTNG Project (TNG hereafter: Marinacci et al. 2018; Naiman et al. 2018; Nelson et al. 2018; Springel et al. 2018; Pillepich et al. 2018b), a suite of magnetohydrodynamical cosmological simulations for the formation of galaxies employing the moving mesh AREPO (Springel 2010) code. The IllustrisTNG simulation is a revised version of the Illustris galaxy formation model (Vogelsberger et al. 2013; Torrey et al. 2014). The IllustrisTNG simulation evolves cold dark matter (DM) and gas from early times to $z = 0$ by solving for the coupled equations of gravity and magnetohydrodynamics (MHD) in an expanding universe. The simulation includes prescriptions that describe the formation of stars, stellar evolution including the return of mass and metals from stars to the interstellar medium (ISM), gas cooling and heating, feedback from stars, and feedback from supermassive black holes (details are given in Weinberger et al. 2017; Pillepich et al. 2018a). Dark matter haloes and their substructures are identified using the SUBFIND algorithm outlined in Springel (2010).

The TNG50 simulation is the highest resolution implementation of the TNG project. This simulation follows the evolution of 2×2160^3 intitial resolution elements inside a cube measuring 35 cMpc h^{-1} on each side, corresponding to a volume of 51.7^3 cMpc^3. This translates to a target mass resolution of $0.85 \times 10^5\,M_\odot$ for the baryonic resolution elements (gas cells and stellar particles), $4.5 \times 10^5\,M_\odot$ for the dark matter resolution elements, a collisionless softening of about 0.3 kpc at $z = 0$, and a minimum gas softening of 74 comoving parsecs. The combination of a cosmological volume with a mass resolution of $0.85 \times 10^5\,M_\odot$ for the baryonic elements makes the TNG50 simulation perfectly suited to study the sizes of galaxies (e.g. Pillepich et al. 2019). The TNG50 simulation adopts a cosmology with $\Omega_m = 0.31$, $\Omega_\Lambda = 0.69$, $\Omega_b = 0.0486$, $h = 0.677$, $\sigma_8 = 0.8159$, $n_s = 0.97$, all consistent with the Planck Collaboration XIII (2016) results.

2.2 Radiative transfer calculations with SKIRT

To model the sub-mm emission of the galaxies from the TNG50 simulation we use the radiative transfer code SKIRT (Baes et al. 2011; Camps, Baes & Saftly 2013; Saftly, Baes & Camps 2014; Camps & Baes 2015). This code traces the scattering and absorption of photon packages by dust until they reach a detector. The code not only calculates an integrated flux for each simulated galaxy (as was for instance explored by Schulz et al. 2020 and Vogelsberger et al. 2020 for IllustrisTNG simulations), but also generates a resolved image of the simulated galaxy at a pre-defined wavelength and resolution (e.g. Cochrane et al. 2019; Rodriguez-Gomez et al. 2019). Here, we largely adopt the same methodology for the radiation transfer calculations as Schulz et al. (2020), which provides additional details. Next, we summarize the methodology and highlight the parameters that were chosen differently from Schulz et al. (2020).

To perform the radiative transfer calculations, we extract the gas cells and stellar particles of the subhalo of interest. To achieve a face-on projection of every subhalo, we then rotate the coordinate systems of the gas and stellar cells/particles to align with the angular momentum vector of the gas in the subhalo (on average the face-on projection results in galaxy sizes 10 per cent more extended than a random projection). Unlike Schulz et al. (2020), we do not include the contribution from young birth clouds to the dust-continuum emission of galaxies. The systematic uncertainty introduced when including birth clouds in SKIRT (e.g. the adopted approach to account for dust in the birth clouds, choosing the age of stars that are still surrounded by birth-clouds, setting the photodissociation-region covering factor and the compaction of the birth clouds) is similar to the uncertainty between including or excluding the birth clouds. Throughout we consider all the gas cells and stellar particles located within 7.5 times the stellar half-mass radius of every subhalo.

The IllustrisTNG simulation suite does not directly follow the dust-abundance of gas cells. Instead, we adopt a dust-to-metal mass ratio (DTM) for gas cells that scales as a function of gas-phase metallicity. In particular, we adopt the relation between DTM and gas-phase metallicity derived for local galaxies by Rémy-Ruyer et al. (2014, for a metallicity-dependent CO-to-H_2 conversion factor, see also De Vis et al. 2019). Rémy-Ruyer et al. (2014) found that DTM quickly increases as a function of metallicity up to a metallicity of 0.4 times solar. At higher metallicities the DTM takes a constant value of 0.32. We assume that this relation is redshift independent, motivated by absorption studies of the dust-to-metal ratio through damped Ly-alpha and gamma-ray absorbers up to $z = 5$ (De Cia et al. 2016; Wiseman et al. 2017; Péroux & Howk 2020), as well as emission-line studies of the dust-to-gas ratio of $z \sim 2$ galaxies (Shapley et al. 2020). The assumption of a redshift-independent relation between dust-to-metal ratio and gas-phase metallicity is also supported by some simulations (cf. Popping, Somerville & Galametz 2017a; Hou et al. 2019; Li, Narayanan & Davé 2019). A dust abundance is only ascribed to gas cells with a temperature less than 75 000 K or particles that are forming stars. We use a Weingartner & Draine (2001) Milky Way Dust prescription to model a mixture of graphite, silicate, and PAH grains. We do not account for dust self-absorption, but checked on a subsample of galaxies that the inclusion of dust self-absorption results in radii that are different by only ∼3 per cent for main-sequence galaxies compared to our fiducial model set-up. In Appendix A, we explore how the choice of the DTM relation influences our results.

As a part of the radiative transfer calculations, SKIRT also provides the dust temperature of every gas cell (see the examples in Fig. 1). This dust temperature corresponds to the average temperature of grains of different species (composition and size) within a cell. This is different a priori from the dust temperature that is observationally derived through SED fitting (see Liang et al. 2019 for a detailed discussion of different definitions of dust temperature). The CMB acts as an additional heating source of the dust and as a background against which the dust-continuum emission of the modelled galaxies is observed (da Cunha et al. 2013). To account for this, we included the effects of the cosmic-microwave background (CMB) following Behrens et al. (2018) and Liang et al. (2019).

For the SKIRT output, we define a wavelength grid of 100 uniformly spaced discrete wavelengths between the rest-frame UV and FIR wavelengths (in log space from 1000 Å to 1 mm). The SKIRT output images at every wavelength are stored in fits images containing 450 pixels on a side.

2.3 TNG50 galaxy selection

In this work, we focus on the dominant population of star-forming galaxies, i.e. those that lie on the star formation main-sequence (SFMS) and above. These are the galaxies that are most likely to be observed in statistical numbers with current sub-mm instrumentation (e.g. Kaasinen et al. 2019). We use the same classification of SFMS galaxies as Schulz et al. (2020), based on the classification used in Pillepich et al. (2019, section 4). Pillepich et al. (2019) calculated the median specific star formation rate (sSFR) inside twice the 3D stellar half-mass radius of galaxies in 0.2 dex wide stellar mass bins running from 10^8 to $10^{10.2}\,M_\odot$. All galaxies with an sSFR with a logarithmic distance (i.e. $\log \mathrm{sSFR} - \log \mathrm{sSFR}_{\mathrm{median}}$) less than −0.5 from the median sSFR were rejected. The process was then repeated until the median converged. A power law was then fitted to the sSFR median to extrapolate the main-sequence to higher stellar masses. All galaxies with a logarithmic distance larger than −0.5 were then classified as being on the main-sequence or above. We do not make a distinction between central and satellite galaxies. For this work, we focus on stellar masses and SFRs within twice the stellar half-mass radius of every subhalo.

We do not include galaxies with a stellar mass less than $10^9\,M_\odot$. This is done to ensure that the individual galaxies are resolved well enough to study their morphological properties. In this work, we focus on galaxies with redshifts $z \leq 5$ to guarantee a decent number of galaxies that meet our initial selection criteria at high redshifts.

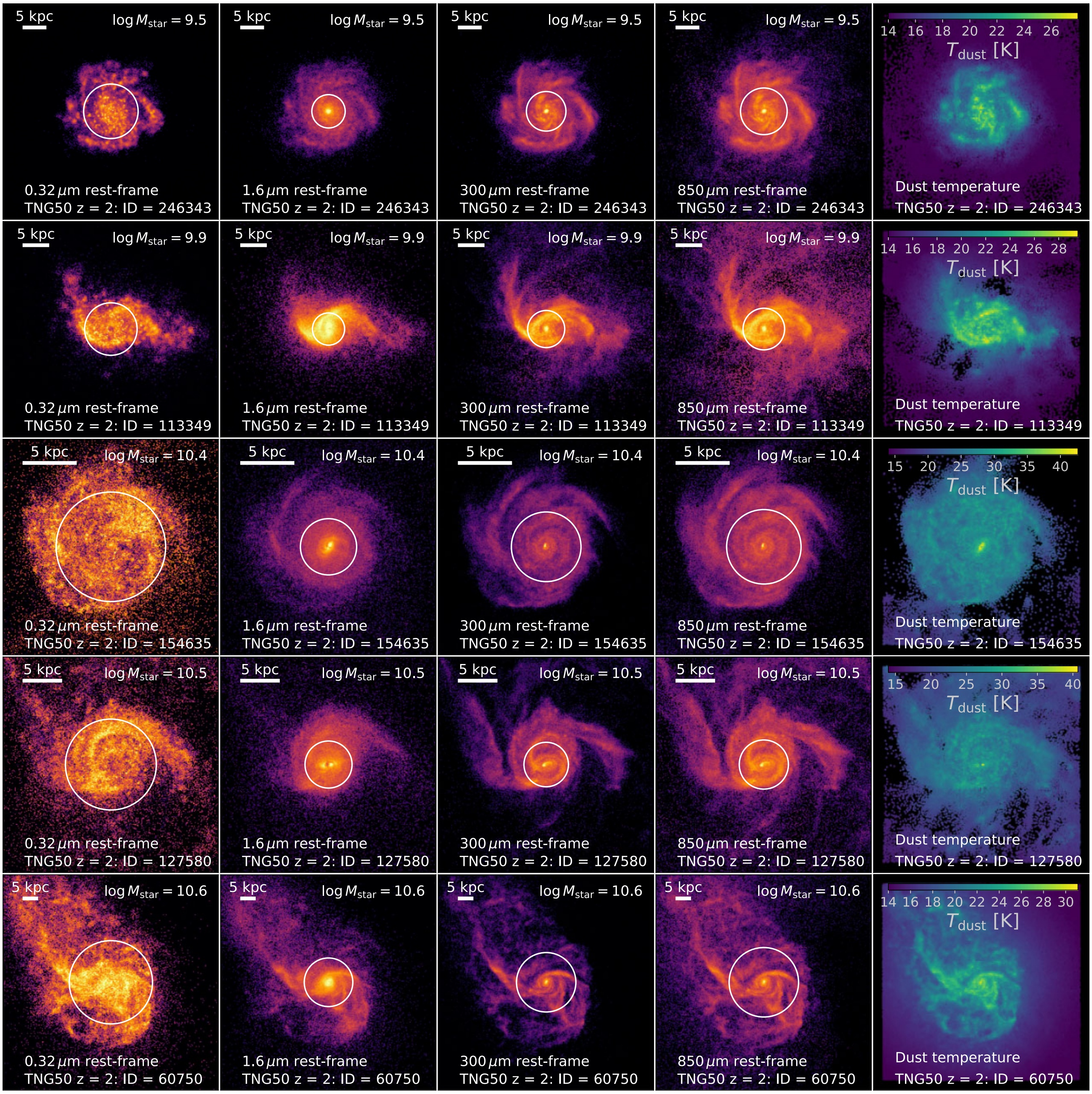

Figure 1. Rest-frame 0.32 μm (left column), 1.6 μm (centre left column), 300 μm (centre column), and 850 μm (centre right column) images of five example galaxies from TNG50 at $z = 2$ with a range of stellar masses. The white circles correspond to the respective half-light radii. The column at the right shows the dust temperature distribution of these galaxies (dust temperatures are weighted by the dust mass along the sightline of every pixel). The morphology and, of interest for this paper, the half-light radii of galaxies vary across wavelengths.

An overview of the number of galaxies considered in this study is given in Table 1.

2.4 Quantifying the size of galaxies

Throughout this paper, the size of a galaxy corresponds to the half-light or half-mass radius of the galaxy. In particular, when we discuss the dust-continuum size of a galaxy we refer to the radius that contains half the light emitted at the respective wavelength. The same is true when we discuss the 1.6 μm size, which corresponds to the radius within which half the emission at an

Table 1. An overview of the number of TNG50 galaxies used in this work.

Redshift z	# TNG50 galaxies: star-forming and $M_* > 10^9\,{\rm M}_{\odot}$
1	1710
2	1149
3	620
4	206
5	76

observed wavelength of 1.6 μm is located. When we discuss the stellar, H_2, or dust size of galaxies we refer to the radius within which half the stellar, H_2, or dust mass is located, respectively. Lastly, when we discuss the SFR size of a galaxy, we refer to the radius within which half the instantaneous star formation of a galaxy takes place. Consistently with the case of dust-continuum, we measure the stellar, H_2, dust, and SFR size of the model galaxies by adopting a face-on projection and only by accounting for gas cells/stellar particles within 7.5 times the stellar half-mass radius. To calculate the H_2 mass of a gas-cell in the TNG50 simulation, we used the methodology presented in Popping et al. (2019), adopting the Gnedin & Kravtsov (2011, hereafter GK), Krumholz (2013, hereafter K13), and Blitz & Rosolowsky (2006, hereafter BR) H_2 recipes (see Popping et al. 2019 for more details).[1] The dust mass corresponds to the metal mass in the ISM multiplied by the dust-to-metal ratio set for every cell as a function of the gas-phase metallicity (see Section 2.2).

We acknowledge that the adopted definition for galaxy size may be different from observationally defined sizes, such as the radius within which 80 per cent of the light is contained (e.g. Mowla et al. 2019), or for example the half-light radius of a Sérsic 2D model fit (e.g. Lange et al. 2015). Additionally, for interferometric data, galaxy sizes can be measured either in the image plane or in the *uv*-plane (e.g. Tadaki et al. 2017; Kaasinen et al. 2020). Furthermore, we have not attempted to account for instrumental effects such as PSF/beam properties and limiting sensitivity. Because these effects are not included, we refrain ourselves from a quantitative comparison with observations both in the figures and in writing.

2.5 Examples

By combining IllustrisTNG and SKIRT we cannot only study the size of the gas components of modelled galaxies, but also the extent of the stellar and dust emission. In Fig. 1, we have included a number of example $z = 2$ modelled galaxies at different wavelengths. We find that the appearance of the galaxies themselves changes as a function of wavelength. At a rest-frame wavelength of 0.32 μm the emission is much more extended than at 1.6, 300, and 850 μm, where we see more centrally concentrated bright emission. This is a reflection of stellar emission being absorbed and re-emitted. From these examples it also becomes clear that the morphology and, of interest for this paper, the sizes of galaxies vary across wavelengths. In the fifth column of Fig. 1, we show the dust temperature distribution of the example galaxies (the dust temperature is weighted by the dust mass along the sightline of each pixel). We find a negative dust temperature gradient across the galaxy disc for all these examples. The negative gradient has implications for the dust-continuum size evolution across FIR wavelengths as we will discuss in the next section.

[1]The IllustrisTNG simulations do not include the chemistry needed to calculate the H_2 mass of gas cells on the fly. Instead, post-processing recipes are adopted to calculate the H_2 mass of gas cells. The K13 and GK recipes are both based on the metallicity, impinging UV field and (surface) density of the gas cells, where the K13 recipe is fully based on analytic calculations and the GK on zoom-in simulations that include the necessary chemistry to follow H_2 formation. The BR recipe is based on an empirical relation between the H_2 fraction and mid-plane pressure of galaxies, where the mid-plane pressure is calculated as a function of the surface density and velocity dispersion of gas and stars.

3 RESULTS

In this section, we present the dust-continuum size of galaxies and how this relates to other galaxy properties.

3.1 The size of galaxies across the sub-mm wavelength regime

Since the shape and peak location of the IR SED depend among others on the temperature distribution of the dust, one may expect differences in the dust-continuum size of galaxies as a function of observed wavelength. Furthermore, an observed wavelength of 850 μm corresponds to a range in rest-frame wavelengths when looking at galaxies at increasing redshifts (e.g. at $z = 4$ an observed wavelength of 850 μm corresponds to a rest-frame wavelength of 170 μm). To better quantify this we first present the dust-continuum size of galaxies for different observed-frame wavelengths.

Fig. 2 shows the ratio between the dust-continuum size of the modelled galaxies at an observed-frame wavelength of 850 μm and the size at other wavelengths running from 300 μm to 2 mm at different redshifts. These ratios are plotted at various redshifts and in bins of stellar mass. Due to the redshifting of the galaxy SED, a fixed observed wavelength probes shorter rest-frame wavelengths with increasing redshift. At all redshifts do we find that the dust-continuum size of galaxies increases with increasing wavelength. This can be explained by dust continuum at shorter wavelengths tracing hotter dust in the centres of galaxies (e.g. Cochrane et al. 2019; Liang et al. 2019), whereas longer wavelengths also trace colder dust that is more extended (see also the last column in Fig. 1). We furthermore find that at $z \geq 1$ dust-continuum sizes estimated in the wavelength range from 500 μm to 2 mm are typically within 20 per cent (10 per cent for galaxies with stellar masses larger than $10^{10}\,M_\odot$) of their 850 μm size. The same conclusion can be drawn for galaxies at $z = 1$ with stellar masses larger than $10^{10}\,M_\odot$. At wavelengths shorter than 500 μm, the size ratio compared to 850 μm on average increases with increasing redshift, whereas this size ratio on average decreases with increasing redshift for size estimates at wavelengths longer than 1 mm. The change in size with observed wavelength is similar to the findings by Cochrane et al. (2019), who found that the dust-continuum size of a single modelled $z \sim 3$ galaxy increases as a function of observed wavelength. We do not find any trend between the various bins of stellar mass.

To first order, the change as a function of wavelength is driven by the dependence of the sub-mm emission strength on the temperature of the dust. At rest-frame wavelengths longer than ∼850 μm, the Rayleigh–Jeans (RJ) tail, the dust-continuum emission is linearly scaled to the mass-weighted dust temperature (Hildebrand 1983). Below a rest-frame wavelength of ∼350 μm the dust becomes optically thick and the strength of the dust-continuum emission depends more strongly on the temperature of the dust. Thus, small deviations in the temperature across the disc will look more pronounced in the dust-continuum emission at a rest-frame wavelength of 200 μm than at 850 μm or 1 mm. A negative dust temperature gradient across the disc (driven for example by hot dust near the galactic centre that is exposed to the hard UV emission of young stars, Cochrane et al. 2019; Liang et al. 2019) therefore naturally translates into smaller sizes at wavelengths below the RJ tail, than at wavelengths above the RJ tail. Indeed, negative gradients in dust temperature across the galaxy discs are seen in Fig. 1. In Fig. 2, we notice changes in disc size already at observed wavelengths of 600 μm and below. This is a natural consequence of the change in the observed SED of galaxies as a function of redshift. At $z = 1$, an observed-frame wavelength of 600 μm already corresponds to a rest-frame wavelength of 300 μm

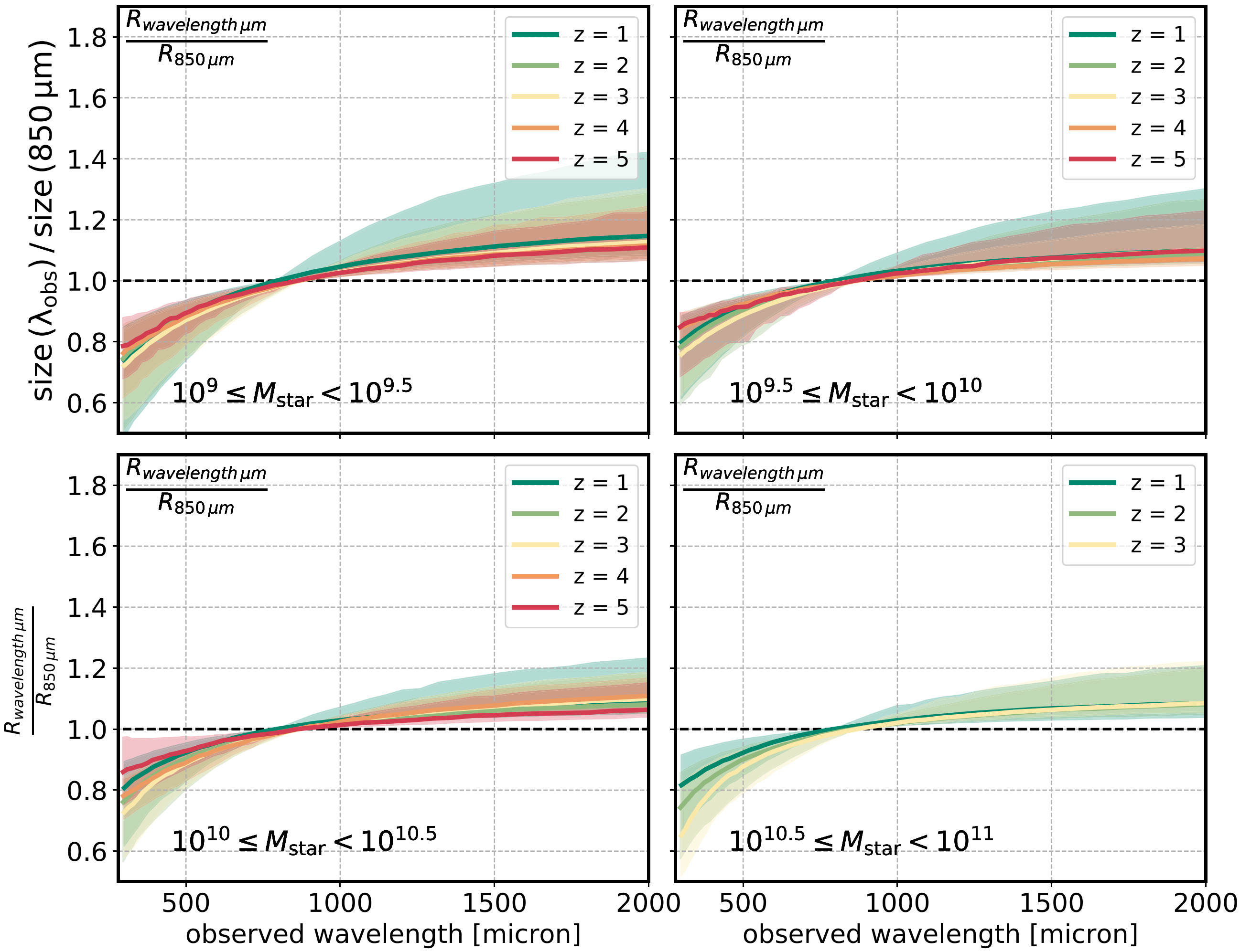

Figure 2. The ratio between the dust-continuum half-light radius of the modelled galaxies at 850 μm and other wavelengths as a function of observed-frame wavelength. The ratios are presented for a range of redshifts and the panels correspond to bins of stellar mass. The solid curves correspond to the median of the distribution, whereas the colour-shaded regions mark the 1σ scatter of the distribution. The black dashed horizontal line corresponds to a ratio of unity. The bottom-right panel does not include galaxies at $z = 4$ and $z = 5$, due to low numbers. The half-light radii of galaxies at wavelengths running from 700 μm to 2 mm (ALMA bands 4 through 8) are similar at the $\lesssim$5–10 per cent level.

(i.e. below the RJ-tail), hence being more sensitive to changes in dust temperature.

Importantly, Fig. 2 also shows that the sizes of galaxies in the observed-wavelength regime running from 700 μm to 2 mm are similar at the $\lesssim$10 per cent level (except for $z = 1$ galaxies with stellar masses less than 10^{10} M$_{\odot}$). This is because the wavelengths are close enough to each other to be dominated by dust at predominantly the same temperatures. This is also encouraging, as these observed-wavelengths roughly correspond to ALMA bands 6 through 8, which are the bands most frequently used for (resolved) continuum studies of galaxies. Sizes estimated in these different bands can thus safely be compared to each other, after accounting for a systematic offset up to a few per cent.

3.2 The stellar mass–dust-continuum size relation of galaxies

In Fig. 3, we show the observed-frame 850 μm size of galaxies as a function of their stellar mass for various redshifts. At $z = 1$ the model predicts a very gentle increase in the 850 μm size of galaxies as a function of stellar mass. At $z = 2$–5 the 850 μm size of galaxies is roughly constant as a function of stellar mass.

At fixed stellar mass the TNG50 + SKIRT model predicts an increase in the observed 850 μm size of galaxies as a function of cosmic time. As we will present in Section 3.4 the 850 μm half-light radius of the galaxies is closely related to the dust half-mass radius and the radius containing half the SFR of the galaxies. This suggests that the evolution at fixed stellar mass of the 850 μm half-light radius is closely related to the build-up of the galaxy disc.

3.3 The ratio between the dust-continuum size and stellar size of galaxies

In the left-hand panel of Fig. 4, we show the ratio between the 850 μm continuum half-light radius and the stellar half-mass radius of modelled galaxies as a function of their stellar mass. The model predicts an increase in this ratio as a function of stellar mass, from ratios around unity at stellar masses of 10^9 M$_{\odot}$ up to ~1.75 at $10^{10.5}$ M$_{\odot}$. Namely, the dust-continuum half-light radius at observed-frame 850 μm is up to ~75 per cent larger than the stellar half-mass

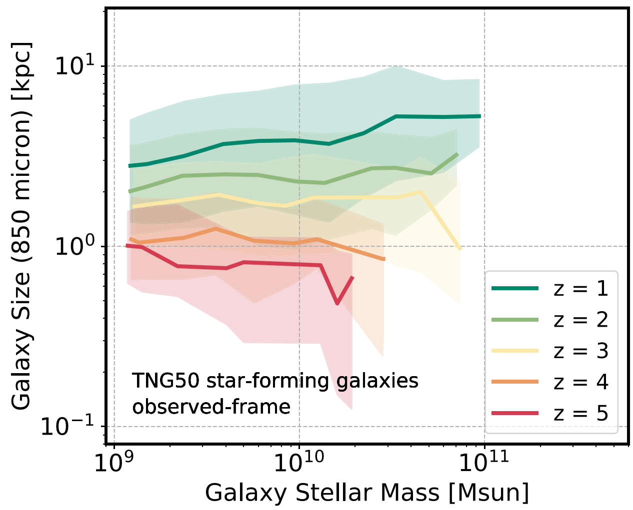

Figure 3. The median dust-continuum size of galaxies at an observed wavelength of 850 μm as a function of stellar mass at different redshifts, as predicted by TNG50 + SKIRT, assuming a Milky Way dust type and a metallicity-dependent dust-to-metal ratio. The model predicts an increase in dust-continuum size at fixed stellar mass with cosmic time. The solid curves correspond to the median of the distribution, whereas the colour-shaded regions mark the 1σ scatter of the distribution.

radius and more so at lower rather than higher redshifts. Moreover, the galaxy-to-galaxy variations, indicated by the shaded areas at 1σ scatter, are very large. At stellar masses smaller than $10^{10}\,M_{\odot}$ we see a gentle increase in the ratio with decreasing redshift.

The prediction that the ratio between 850 μm half-light and stellar half-mass radii is typically around or larger than one seems to be in conflict with current observations. However, the observations do not probe the stellar mass distribution directly, but are commonly measured using an NIR filter (for instance the *K* and *H* band in van der Wel et al. 2014). To allow for a better comparison with the observations, we show the ratio between the 850 μm and 1.6 micron observed-frame half-light radii of the modelled galaxies as a function of their stellar mass and redshift in the right-hand panel of Fig. 4. The model predicts a very gentle decrease in this ratio as a function of stellar mass at redshifts $z \leq 2$, whereas at the other redshifts the predicted ratio is roughly constant. Furthermore, the model predicts an increase in the ratio with cosmic time. Most importantly, the ratio between the 1.6 and 850 μm half-light radii is around one at $z = 1$ and decreases towards higher redshifts, down to ratios of 0.3 at $z = 5$. This is in much better qualitative agreement with the observations than the predicted ratio between 850 μm and stellar half-mass radius (e.g. Barro et al. 2016; Tadaki et al. 2020). In Section 4.1, we will discuss in more detail the reasons behind this different behaviour.

3.4 The ratio between the dust-continuum size and dust and SFR size of galaxies

In the left-hand panel of Fig. 5, we present the ratio between the observed-frame dust-continuum half-light radius and the dust half-mass radius of galaxies as a function of their stellar mass and redshift. We find that the dust-continuum half-light radius is smaller than the dust half-mass radius at stellar masses less than $10^{10}\,M_{\odot}$ with a typical ratio of 0.8, whereas it is close to unity for more massive galaxies.

In the right-hand panel of Fig. 5, we show the predicted ratio between the observed-frame 850 μm size of galaxies and the radius containing half the SFR as a function of stellar mass and redshift. We find that this ratio gently increases with stellar mass and has no significant redshift evolution. The median ratio runs from ~0.85 to ~1.2 in the stellar mass range from 10^9 to $10^{10.8}\,M_{\odot}$.

The presented results suggest that the dust-continuum emission closely traces the underlying dust mass as well as the location where star formation happens that heats up the dust. Here, it is relevant to point out that model assumptions do matter. In a test where we included the effects of birth clouds following the approach outlined in Schulz et al. (2020), we found that the dust-continuum closely traces the star formation distribution of the galaxies, but is more compact by about 25 per cent than the dust mass distribution over the entire stellar mass range.

3.5 The ratio between the dust-continuum half-light radius and H_2 half-mass radius

In Fig. 6, we plot the ratio between the observed-frame 850 μm size of galaxies and the H_2 half-mass size as a function of stellar mass and redshift when adopting the Gnedin & Kravtsov (2011, GK), Krumholz (2013, K13), and Blitz & Rosolowsky (2006, BR) H_2 recipes. We find that this ratio on average decreases with redshift, independent of stellar mass and adopted H_2 recipe. For all three recipes, at $z = 1$ the ratio is typically close to one for galaxies with stellar masses larger than $10^{10}\,M_{\odot}$. At $z = 2$ the median ratio is ~0.9 at these stellar masses, whereas it decreases down to ~0.7 for galaxies with stellar masses of a few times $10^{10}\,M_{\odot}$ at $z \geq 4$.

At stellar masses below $10^{10}\,M_{\odot}$ the model predicted ratio between the observed-frame 850 μm size of galaxies and the H_2 half-mass size is more dependent on the adopted H_2 recipe. When adopting the GK and K13 recipes, we find a gentle decrease in the ratio between 850 μm size of galaxies and the H_2 half-mass size as a function of stellar mass. When adopting the BR recipe the ratio is essentially constant with stellar mass, and we only see a redshift dependence. It is worthwhile to mention that both the GK and K13 recipes include a metallicity dependence, whereas the BR recipe does not. A metallicity gradient (with lower metallicities in the outskirts of TNG50 galaxies, see Hemler et al. 2021) naturally leads to changes in the H_2 half-mass size of the model galaxies as the lower metallicities at larger radii prohibit the efficient formation of H_2.

Despite the difference between the H_2 recipes, overall we find that at stellar masses larger than $10^{10}\,M_{\odot}$ the 850 μm size of the modelled galaxies is smaller by approximately 10–30 per cent than the H_2 half-mass size at $z \geq 2$. Furthermore, we find that galaxies at $z = 1$ with stellar masses less than $10^{10}\,M_{\odot}$ have dust-continuum radii larger than the radius that contains half the H_2 mass (up to 50–75 per cent for the metallicity-dependent H_2 recipes GK and K13). A future direction of this conclusion is to compare the dust-continuum emission to the CO emission of galaxies, allowing for a more direct comparison with observations.

4 DISCUSSION

4.1 What drives the compact distribution of dust emission in galaxies?

In Section 3.3, we showed that the ratio between the dust-continuum half-light radius of galaxies and their stellar half-mass size is typically above unity. The ratio with the 1.6 μm half-light radius of galaxies is typically below unity for galaxies at $z \geq 2$ and decreases as a function

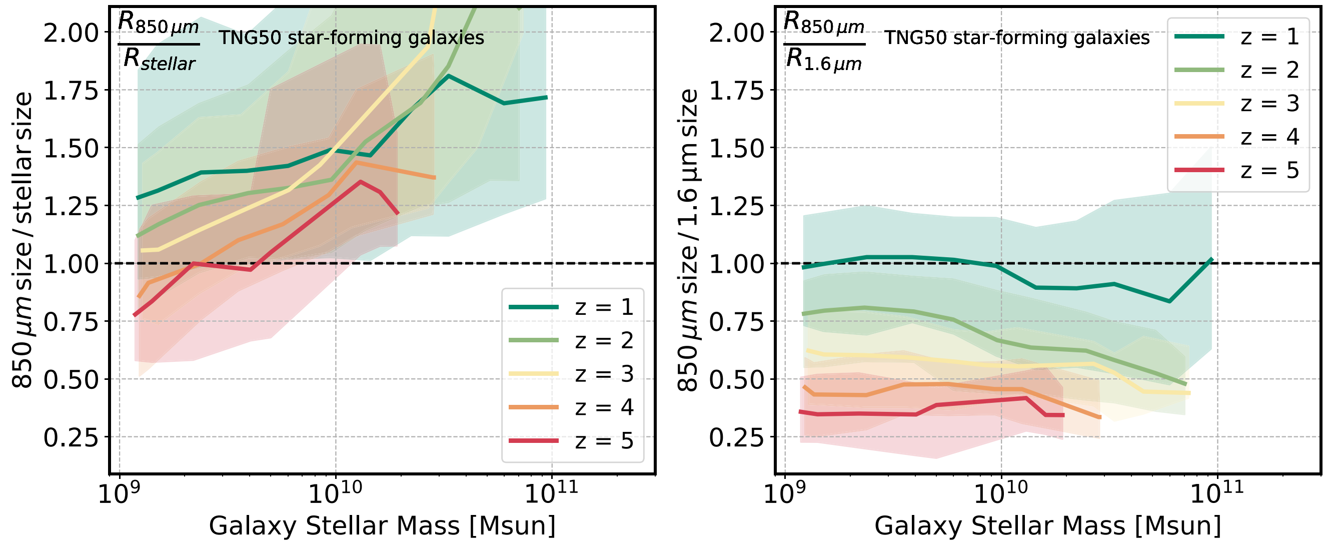

Figure 4. Left-hand panel: The ratio between dust-continuum size of galaxies at an observed wavelength of 850 μm and the stellar half-mass radius as a function of stellar mass at different redshifts. Right-hand panel: The ratio between dust-continuum size of galaxies at an observed wavelength of 850 μm and the 1.6 μm half-light radius as a function of stellar mass at different redshifts, the latter approximating the stellar light radial extent of galaxies in *H* band. The solid curves correspond to the median of the distribution, whereas the colour-shaded regions mark the 1σ scatter of the distribution. The black dashed horizontal line corresponds to a ratio of unity. The observed-frame 850 μm emission is typically more extended than the stellar mass, but more compact than the observed-frame 1.6 μm emission.

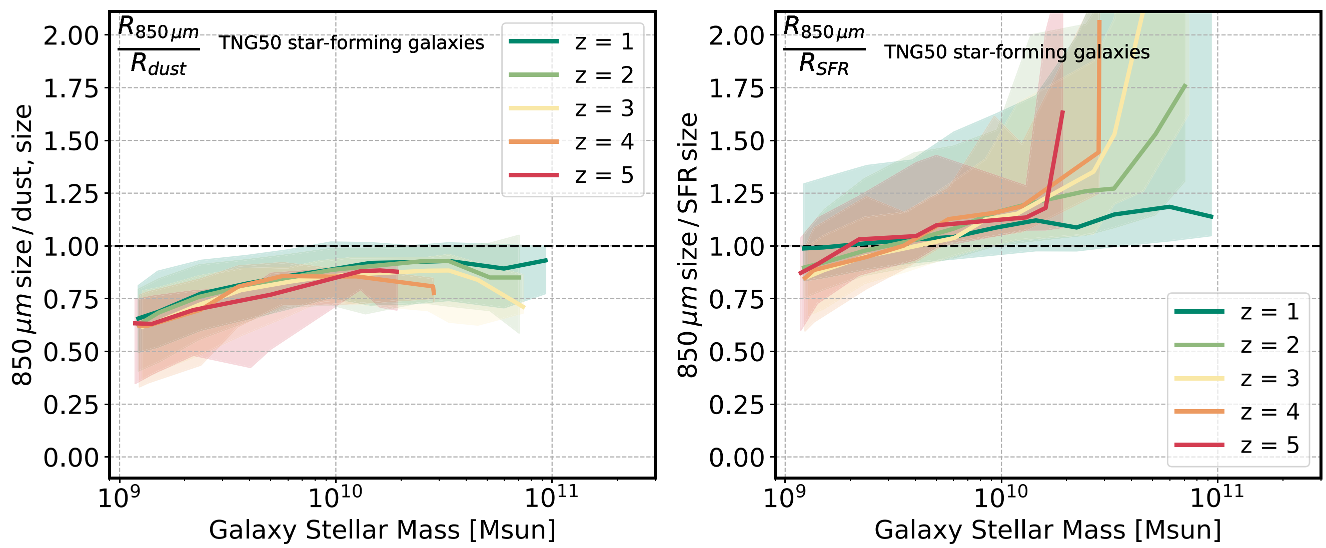

Figure 5. Left-hand panel: The ratio between dust-continuum half-light radius of galaxies at an observed wavelength of 850 μm and the dust half-mass radius as a function of stellar mass at different redshifts. Right-hand panel: The ratio between dust-continuum half-light radius of galaxies at an observed wavelength of 850 μm and the radius containing half of the SFR as a function of stellar mass at different redshifts. The solid curves correspond to the median of the distribution, whereas the colour-shaded regions mark the 1σ scatter of the distribution. The black dashed horizontal line corresponds to a ratio of unity. The dust-continuum half-light radius is more compact than the dust half-mass radius and is similar to the radius containing half the SFR.

of redshift, so that galaxies observed in dust-continuum appear progressively smaller than in *H*-band stellar light at progressively higher redshifts. The latter is in agreement with observations that have also suggested that the dust-continuum sizes of galaxies are more compact than their observed NIR sizes (e.g. Barro et al. 2016; Fujimoto et al. 2017; Calistro Rivera et al. 2018; Lang et al. 2019; Rujopakarn et al. 2019; Tadaki et al. 2020). Here, we aim to give more insight into the origin of the compact dust emission compared to the 1.6 μm emission.

An observed wavelength of 1.6 μm corresponds to increasingly bluer rest-frame wavelengths as a function of redshift. As a result, the effect of dust-obscuration of the observed 1.6 μm emission becomes increasingly more important as the redshift increases. For example, at $z > 3$ the observed 1.6 μm emission already corresponds to the UV regime, in which the obscuration by dust plays an important role. The attenuation of stellar emission by dust may thus play an important role in determining the observed 1.6 μm morphology of galaxies. To examine this in more detail we reran the radiative transfer models, but

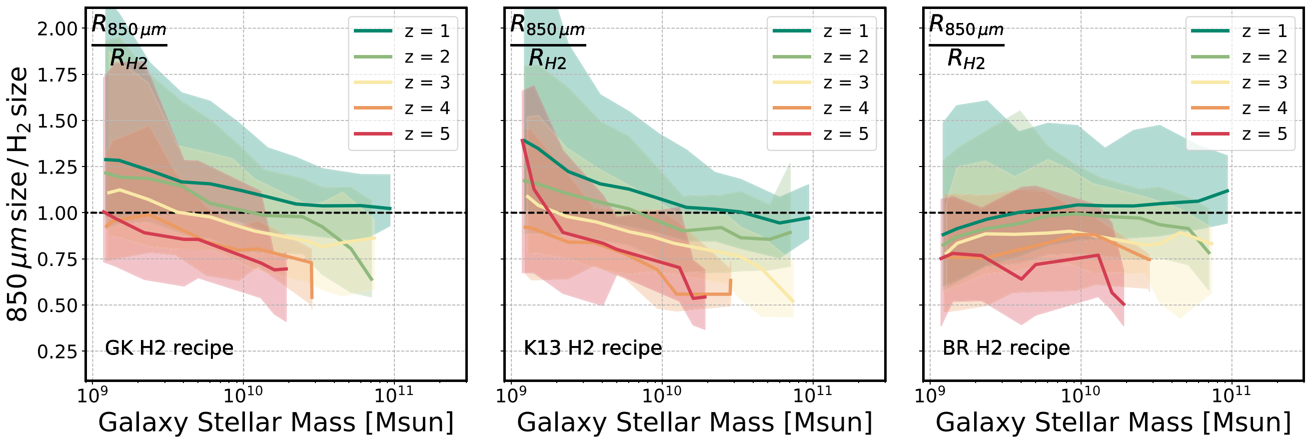

Figure 6. The ratio between dust-continuum half-light radius of galaxies at an observed wavelength of 850 μm and the molecular hydrogen half-mass radius as a function of stellar mass at different redshifts for the GK (Gnedin & Kravtsov 2011, left), K13 (Krumholz 2013, middle), and the BR (Blitz & Rosolowsky 2006, right) H_2 recipes. The solid curves correspond to the median of the distributions, whereas the colour-shaded regions mark the 1σ scatter of the distributions. The black dashed horizontal line corresponds to a ratio of unity. Above stellar masses of 10^{10} M$_\odot$ the predicted ratios for $z \geq 2$ galaxies are typically below one (smaller than 0.75), independent of the adopted H_2 recipes. At lower stellar masses the ratios predicted when adopting the three H_2 recipes differ.

without including dust. As a consequence, the stellar emission is not absorbed by dust *and* therefore no obscured emission is re-emitted in the IR either. In Fig. 7, we show the same $z = 2$ example galaxies as in Fig. 1 (top half of the figure), but at an observed wavelength of 1.6 μm (corresponding to a rest-frame wavelength of ∼0.53 μm). We furthermore present five galaxies at $z = 5$ (bottom half of the figure). The galaxies are shown when including dust attenuation (top row) and when not including dust attenuation (middle row). The central region of most of the example galaxies, both at $z = 2$ and $z = 5$, is much brighter at an observed wavelength of 1.6 μm in the bottom row than in the top row, i.e. it is brighter when ignoring dust obscuration. Only for the least massive galaxy do we hardly see any change in the brightness of the central region (due to a lack of dust obscuration in low-mass galaxies to begin with, Whitaker et al. 2017). The difference in profile becomes clearer in the bottom rows of Fig. 7. Here, we show the 1.6 μm radial light profile of the example galaxies when including dust attenuation and when not including dust attenuation. For all example galaxies, the shape of the profiles is flatter when including dust attenuation (and even sometimes includes a dip in the centre). The change in central brightness naturally results in a different half-light radius for these objects when including dust absorption versus when not including dust absorption.

In Fig. 8, we show the ratio between the 1.6 μm observed-frame half-light radius of galaxies and the stellar half-mass radius when including dust attenuation (left-hand panel) and when not including dust attenuation (central panel). For the former scenario, we find that the 1.6 μm half-light radius is more extended than the stellar half-mass radius. The ratio increases as a function of redshift and stellar mass. For the latter scenario (no dust attenuation) the model predicts a ratio between the 1.6 μm half-light radius and the stellar half-mass radius around unity, independent of stellar mass and redshift. Indeed, the ratio between the two scenarios (right-hand panel of Fig. 8) is also larger than one and increases with stellar mass and redshift. The redshift trend is there because the observed-frame 1.6 μm emission probes shorter rest-frame wavelengths that are more sensitive to dust obscuration with increasing redshift. Future observations focusing on the dust-continuum size of galaxies compared to the *H*-band size at various redshifts may actually directly test this prediction.

The predictions presented in Figs 7 and 8 suggest the following scenario. The presence of dust attenuates the central bright 1.6 μm emission of galaxies. Because the central bright component is attenuated, the half-light radius of the galaxies becomes larger compared to the scenario where no dust attenuation takes place. Thus, although the unobscured 1.6 μm emission very closely follows the stellar distribution, dust attenuation skews the light profile. This becomes increasingly more important at higher redshifts, since the 1.6 μm emission traces rest-frame wavelengths that are increasingly more susceptible to dust attenuation. The dust emission on the other hand dominates at the locations where the attenuation is strongest (i.e. most light is reprocessed). This is also visible in Fig. 1, where the dust-continuum emission at rest-frame 300 and 850 μm is more centrally concentrated than the emission at UV wavelengths.

The above suggested scenario provides a natural explanation to why the observed dust emission appears more compact than the observed NIR emission of galaxies in $z > 2$ galaxies. Dust obscuration increases the observed optical/NIR half-light radius compared to the distribution of the dust-continuum emission. Our results suggest that the compact dust distribution is not necessarily a sign of the build-up of a dense central stellar component. On the contrary, on average the predicted dust-continuum half-light radius is similar to the stellar half-mass radius, indicating that the dust-obscured star formation follows the stellar mass distribution relatively closely. This is a common feature of galaxies on the main-sequence and not a peculiarity belonging to a subclass of main-sequence galaxies. This conclusion does not depend strongly on the underlying choices made for the radiative transfer calculations (e.g. the inclusion of birth clouds).

The presented conclusion has implications for future observations of the resolved dust-continuum distribution of galaxies and their interpretation. When planning ALMA observations aiming at resolving the dust-continuum emission of galaxies, one should expect the galaxies to be smaller than inferred from optical/NIR observations (about 25 per cent at $z = 2$ and more than 50 per cent at $z = 5$). This means that to resolve the dust-continuum emission of galaxies at $z > 1$, more extended ALMA configurations may be necessary than one would conclude from the optical/NIR morphology.

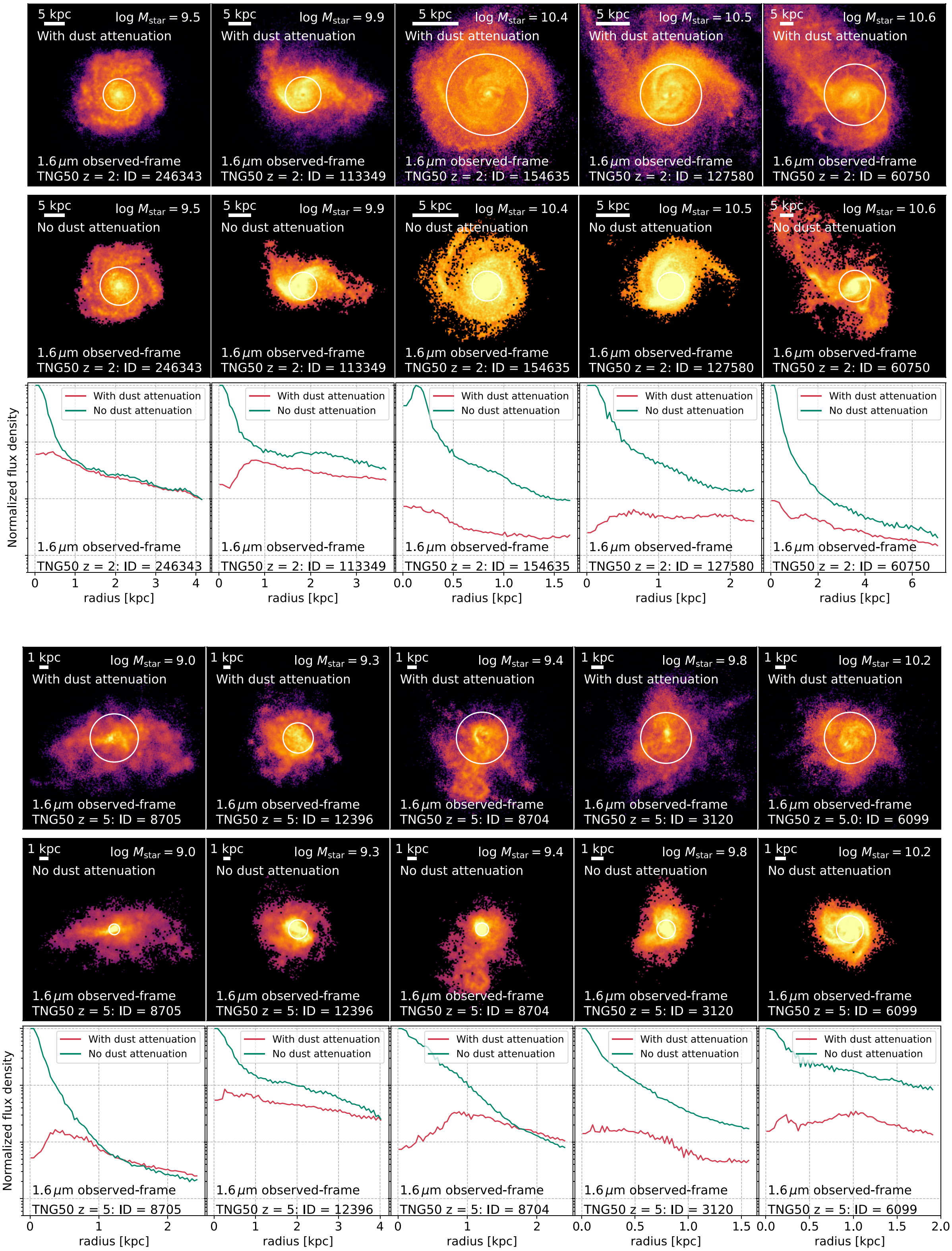

Figure 7. Poststamps of the observed-frame 1.6 µm emission of the example galaxies at z = 2 (top three rows) displayed in Fig. 1 and z = 5 (bottom three rows). For each redshift, the top row corresponds to a SKIRT run including the effects of dust attenuation, whereas the middle row corresponds to the scenario where no dust attenuation is applied. The white circles correspond to the respective half-light radii. For individual galaxies, the top and middle row have the same colour scaling. It becomes clear that dust obscures the central bright component of the stellar emission. The bottom row shows the 1.6 µm light profile of the same galaxies when including (red) and not including (green) dust attenuation. The radial profiles are normalized to the peak flux density of the profile without dust attenuation. The shape of the profiles is flatter when including dust attenuation, naturally extending the half-light radius.

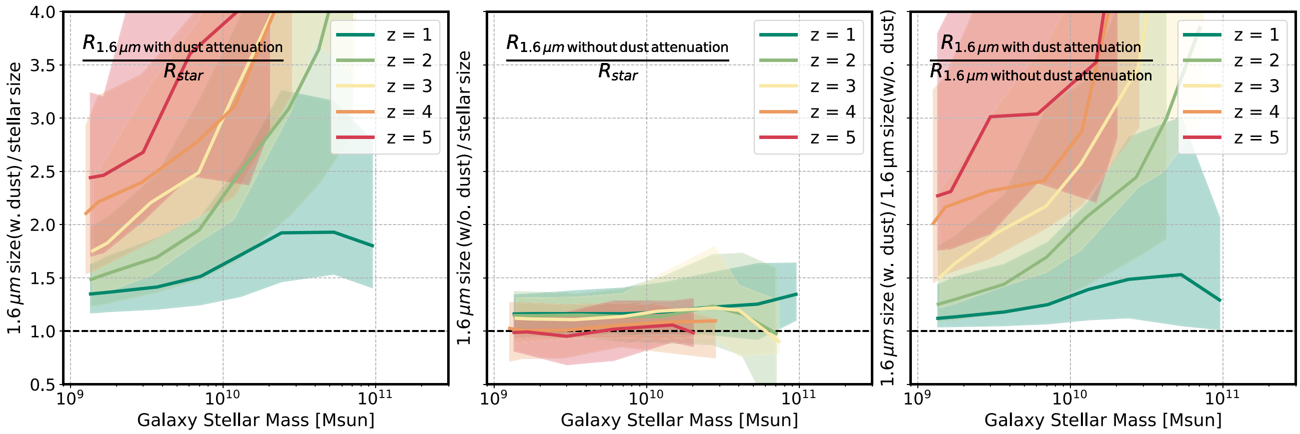

Figure 8. Left: The ratio between observed-frame 1.6 μm half-light radius of the modelled galaxies and their stellar half-mass radius as a function of stellar mass and redshift, including the effects of dust attenuation as in Fig. 7. Centre: The ratio between 1.6 μm half-light radius of the modelled galaxies and their stellar half-mass radius as a function of stellar mass and redshift, not including the effects of dust attenuation. Right: The ratio between the 1.6 μm half-light radius of galaxies with and without including dust attenuation plotted as a function of stellar mass and redshift. The solid curves correspond to the median of the distribution, whereas the colour-shaded regions mark the 1σ scatter of the distribution. The black dashed horizontal line corresponds to a ratio of unity.

4.2 Does the single-band dust-continuum emission of galaxies trace the H_2 distribution?

In recent years, the integrated single-band dust-continuum emission of galaxies has often been used as a tracer of the H_2 mass of galaxies (e.g. Eales et al. 2012; Bourne et al. 2013; Scoville et al. 2013, 2016; Schinnerer et al. 2016; Hughes et al. 2017). In this work (Fig. 6), we showed that our model predicts ratios between the 850 μm observed-frame half-light size and H_2 half-mass size of galaxies of 0.75 and below for massive galaxies ($M_{\rm star} > 10^{10}$ M$_\odot$) at $z \geq 2$ (independent of the adopted H_2 recipe). At these redshifts galaxies with these masses are typically the ones most easily to resolve by ALMA due to their brightness. The low ratio suggests that the resolved 850 μm dust-continuum emission of galaxies traces only the central component of the H_2 mass distribution at $z > 2$.

Observations also found that the dust-continuum emission is more compact than the CO emission tracing H_2 (Hodge et al. 2015; Chen et al. 2017; Calistro Rivera et al. 2018; Kaasinen et al. 2020). Even though we do not provide predictions for CO emission directly, our predictions suggest that this is true for the majority of main-sequence galaxies and that the dust becomes increasingly more compact compared to H_2 with increasing redshift. We have demonstrated in the right-hand panel of Fig. 5 that the dust-continuum emission closely follows the radius containing half of the star formation. The UV photons from the star-forming regions heat up the dust and allow the dust to efficiently emit in the sub-mm wavelength regime. Thus, in our model the underlying driver of the ratio between 850 μm and H_2 mass is actually the ratio in the size of the star-forming region and the H_2 mass. We checked that this ratio indeed closely follows the trend shown in Fig. 6.

In the presented simulation the SFR of a gas cell is not coupled to its H_2 mass (since the H_2 mass is calculated in post-processing). Therefore, there does not need to be a linear relation between the H_2 mass of a cell and its SFR. It is thus possible for a cell to contain molecular hydrogen, with only little or no star formation at all (see Diemer et al. 2018 and Popping et al. 2019). This naturally allows for a more extended H_2 disc than SFR or dust-continuum disc. But more importantly, dust strongly emits radiation at locations where the dust is heated by emission from young stars (resulting in high dust temperatures). These do not necessarily overlap with the locations where the H_2 mass and CO emission dominate. In a future work, we will focus in more detail on the highly resolved emission properties of galaxies.

5 SUMMARY AND CONCLUSIONS

In this work, we have presented predictions for the dust-continuum half-light radius of simulated galaxies, obtained by coupling the radiative transfer code SKIRT to the output of the TNG50 simulation and by adopting as our fiducial ansatz a Milky Way dust type and a metallicity-dependent dust-to-metal ratio (based on Rémy-Ruyer et al. 2014). The selected simulated galaxies all lie near the star-forming main-sequence, have stellar masses between 10^9 and 10^{11} M$_\odot$ and fall in the redshift range $1 < z < 5$. We compared the dust-continuum half-light radii of the simulated galaxies (with special focus on observed-frame 850 μm) with their stellar, dust, and H_2 half-mass radii and the radius containing half the star formation. Our results pertaining to TNG50 galaxies can be summarized as follows.

(i) The dust-continuum size of a galaxy is roughly constant (within ∼5–10 per cent) as a function of wavelength running from 700 μm to 1 mm (corresponding to ALMA bands 6 though 8). The sizes are within ∼20 per cent of each other in the wavelength regime going from 500 μm to 2 mm (roughly corresponding to ALMA bands 4 though 9, see Fig. 2).

(ii) The predicted 850 μm half-light radius of galaxies increases as a function of cosmic time and is constant (shows a very mild increase) as a function of stellar mass for galaxies at $z \geq 2$ ($z = 1$, see Fig. 3).

(iii) The predicted observed-frame 850 μm half-light radius is smaller than the observed-frame 1.6 μm half-light radius (corresponding to the *H*-band size), as also seen in observations (Fig. 4). The ratio between the half-light radii decreases as a function of redshift, from 0.8 at $z = 1$ to less than 0.6 at $z \geq 2$ for galaxies more massive than 10^{10} M$_\odot$. This ratio is driven by the obscuration of the 1.6 μm emission, increasing the observed 1.6 μm half-light radius of galaxies (Fig. 8). The relative compactness increases with redshift, because the observed 1.6 μm emission corresponds to increasingly bluer rest-frame wavelengths that are more affected by dust attenuation as a function of redshift.

(iv) On the other hand, the 850 μm half-light radius is typically larger (similar) than the stellar half-mass radius at $z \leq 3$ ($z \geq 4$; Fig. 4).

(v) The previous points are a common feature of galaxies on the main-sequence of star formation. Combined, they suggest that the relatively compact dust distribution seen in observations is not necessarily a sign of the dust-obscured build-up of a central dense stellar component, rather a reflection of the change of the stellar light profile of galaxies by dust.

(vi) The 850 μm half-light radius of galaxies is a good tracer of the radius containing half the star formation for galaxies with stellar masses less than $10^{10}\,M_{\odot}$, whereas the sizes are up to 20 per cent larger for more massive galaxies. Similarly, the 850 μm half-light radius closely follows the radius containing half the dust mass of galaxies with stellar masses more massive than $10^{10}\,M_{\odot}$, whereas at lower masses the 850 μm half-light radius is up to 20 per cent smaller. These results confirm that that the dust-continuum emission is very closely related to the location and heating of dust by star formation in galaxies (Fig. 5).

(vii) The 850 μm half-light radius is not always a good tracer of the resolved H_2 size of galaxies at $z \geq 2$ (Fig. 6). For galaxies with stellar masses larger than $10^{10}\,M_{\odot}$ the dust-continuum size is 0.75 times smaller than the H_2 half-mass radius at $z = 2$, and this fraction further decreases towards higher redshifts. The dust emission strongly correlates with locations with the highest dust temperatures, which are not necessarily the locations where most H_2 is located.

(viii) The 850 μm half-light radius of galaxies is about 25 per cent smaller than the dust half-mass radius throughout the studied ranges of $10^{9-11}\,M_{\odot}$ and $1 < z < 5$ in mass and redshift, respectively (Fig. 5). This indicates that the dust emission is not a robust tracer of the underlying dust mass, driven by the dust emission dominating in regions with high dust temperatures.

5.1 Implications for (future) observations

The presented results have a number of implications for (the interpretation of) future observations:

(i) Efforts to resolve the dust-continuum emission of large numbers of galaxies will require ALMA antenna configurations that resolve the galaxy at scales significantly smaller than their optical/NIR size.

(ii) The use of the dust-continuum emission of galaxies as a reliable tracer of the resolved H_2 and dust mass distribution will require multiband coverage of the dust SED to account for changes in the dust temperature (and thus the strength of dust emission) across the galaxy discs.

(iii) The dust-continuum sizes of galaxies at $1 < z < 5$ as determined from ALMA observations using bands 4 through 7 can safely be compared to each other.

The results presented in this work can serve as a guidance for future observations of the dust continuum in galaxies. We believe this is particularly timely given current and ongoing efforts with ALMA. We thus look forward to future observations further constraining our model predictions for the resolved dust-continuum properties of main-sequence galaxies, pushing forward the connection between gas and star formation in galaxies over cosmic time.

ACKNOWLEDGEMENTS

GP thanks Lichen Liang, Christoph Behrens, Connor Bottrell, Roberto Decarli, Rob Ivison, Gandhali Joshi, Georgios Magdis, and Fabian Walter for useful discussions. We furthermore thank the referee for a constructive report. Simulations for this work were performed on the Isaac supercomputer at the Max Planck Computing and Data Facility, while the TNG50 flagship run was realized with compute time granted by the Gauss Centre for Super-computing (GCS) under GCS Large-Scale Project GCS-DWAR (2016; PIs Nelson/Pillepich). MK acknowledges support from the International Max Planck Research School for Astronomy and Cosmic Physics at Heidelberg University (IMPRS-HD). FM acknowledges support through the Program 'Rita Levi Montalcini' of the Italian MUR. DN acknowledges funding from the Deutsche Forschungsgemeinschaft (DFG) through an Emmy Noether Research Group (grant number NE 2441/1-1). We acknowledge use of the `python` programming language version 3.7, available at http://www.python.org, Astropy (Astropy Collaboration 2013; Price-Whelan et al. 2018), Matplotlib (Hunter 2007), NumPy (Oliphant 2006; Van Der Walt, Colbert & Varoquaux 2011), SciPy (Virtanen et al. 2020), and Seaborn (Waskom et al. 2017).

DATA AVAILABILITY

The data that support the findings of this study are available on request from the corresponding author. All data pertaining to the IllustrisTNG project, including the TNG50 run analysed here, are already openly available (Nelson et al. 2019a) and can be retrieved from the IllustrisTNG website, at www.tng-project.org/data.

REFERENCES

Aravena M. et al., 2020, ApJ, 901, 79
Astropy Collaboration, 2013, A&A, 558, A33
Baes M., Camps P., 2015, Astron. Comput., 12, 33
Baes M., Verstappen J., De Looze I., Fritz J., Saftly W., Vidal Pérez E., Stalevski M., Valcke S., 2011, ApJS, 196, 22
Barro G. et al., 2016, ApJ, 827, L32
Behrens C., Pallottini A., Ferrara A., Gallerani S., Vallini L., 2018, MNRAS, 477, 552
Bertemes C. et al., 2018, MNRAS, 478, 1442
Blitz L., Rosolowsky E., 2006, ApJ, 650, 933 (BR)
Bourne N. et al., 2013, MNRAS, 436, 479
Calistro Rivera G. et al., 2018, ApJ, 863, 56
Camps P., Baes M., 2015, Astron. Comput., 9, 20
Camps P., Baes M., Saftly W., 2013, A&A, 560, A35
Camps P., Trayford J. W., Baes M., Theuns T., Schaller M., Schaye J., 2016, MNRAS, 462, 1057
Chen C.-C. et al., 2017, ApJ, 846, 108
Cochrane R. K. et al., 2019, MNRAS, 488, 1779
da Cunha E. et al., 2013, ApJ, 766, 13
Daddi E., Dannerbauer H., Elbaz D., Dickinson M., Morrison G., Stern D., Ravindranath S., 2008, ApJ, 673, L21
De Cia A., Ledoux C., Mattsson L., Petitjean P., Srianand R., Gavignaud I., Jenkins E. B., 2016, A&A, 596, A97
De Vis P. et al., 2019, A&A, 623, A5
Diemer B. et al., 2018, ApJS, 238, 33
Eales S. et al., 2012, ApJ, 761, 168
Fujimoto S., Ouchi M., Shibuya T., Nagai H., 2017, ApJ, 850, 83
Gnedin N. Y., Kravtsov A. V., 2011, ApJ, 728, 88 (GK)
Groves B. A. et al., 2015, ApJ, 799, 96
Gullberg B. et al., 2019, MNRAS, 490, 4956
Hemler Z. S. et al., 2021, MNRAS, 506, 3024
Hildebrand R. H., 1983, Q. J. R. Astron. Soc., 24, 267

Hodge J. A., da Cunha E., 2020, R. Soc. Open Sci., 7, 200556
Hodge J. A. et al., 2013, ApJ, 768, 91
Hodge J. A., Riechers D., Decarli R., Walter F., Carilli C. L., Daddi E., Dannerbauer H., 2015, ApJ, 798, L18
Hodge J. A. et al., 2019, ApJ, 876, 130
Hopkins P. F. et al., 2018, MNRAS, 480, 800
Hou K.-C., Aoyama S., Hirashita H., Nagamine K., Shimizu I., 2019, MNRAS, 485, 1727
Hughes T. M. et al., 2017, MNRAS, 468, L103
Hunter J. D., 2007, Comput. Sci. Eng., 9, 90
Ikarashi S. et al., 2015, ApJ, 810, 133
Jonsson P., 2006, MNRAS, 372, 2
Kaasinen M. et al., 2019, ApJ, 880, 15
Kaasinen M. et al., 2020, ApJ, 899, 37
Karim A. et al., 2013, MNRAS, 432, 2
Krumholz M. R., 2013, MNRAS, 436, 2747 (K13)
Lagos C. d. P. et al., 2019, MNRAS, 489, 4196
Lang P. et al., 2019, ApJ, 879, 54
Lange R. et al., 2015, MNRAS, 447, 2603
Li Q., Narayanan D., Davé R., 2019, MNRAS, 490, 1425
Liang L., Feldmann R., Faucher-Giguère C.-A., Kereš D., Hopkins P. F., Hayward C. C., Quataert E., Scoville N. Z., 2018, MNRAS, 478, L83
Liang L. et al., 2019, MNRAS, 489, 1397
Liang L., Feldmann R., Hayward C. C., Narayanan D., Çatmabacak O., Kereš D., Faucher-Giguère C.-A., Hopkins P. F., 2021, MNRAS, 502, 3210
Lovell C. C., Geach J. E., Davé R., Narayanan D., Li Q., 2021, MNRAS, 502, 772
McKinnon R., Torrey P., Vogelsberger M., 2016, MNRAS, 457, 3775
Marinacci F. et al., 2018, MNRAS, 480, 5113
Millard J. S., Diemer B., Eales S. A., Gomez H. L., Beeston R., Smith M. W. L., 2021, MNRAS, 500, 871
Mowla L. A. et al., 2019, ApJ, 880, 57
Naiman J. P. et al., 2018, MNRAS, 477, 1206
Narayanan D. et al., 2021, ApJS, 252, 12
Nelson D. et al., 2018, MNRAS, 475, 624
Nelson D. et al., 2019a, Computat. Astrophys. Cosmol., 6, 2
Nelson D. et al., 2019b, MNRAS, 490, 3234
Nelson E. J. et al., 2019c, ApJ, 870, 130
Noeske K. G. et al., 2007, ApJ, 660, L43
Oliphant T. E., 2006, A guide to NumPy, Vol. 1. Trelgol Publishing, USA
Péroux C., Howk J. C., 2020, ARA&A, 58, 363
Pillepich A. et al., 2018a, MNRAS, 473, 4077
Pillepich A. et al., 2018b, MNRAS, 475, 648
Pillepich A. et al., 2019, MNRAS, 490, 3196
Planck Collaboration XIII, 2016, A&A, 594, A13
Popping G., Somerville R. S., Galametz M., 2017a, MNRAS, 471, 3152
Popping G. et al., 2017b, A&A, 602, A11
Popping G. et al., 2019, ApJ, 882, 137
Price-Whelan A. M. et al., 2018, AJ, 156, 123
Privon G. C., Narayanan D., Davé R., 2018, ApJ, 867, 102
Rémy-Ruyer A. et al., 2014, A&A, 563, A31
Rodriguez-Gomez V. et al., 2019, MNRAS, 483, 4140
Rujopakarn W. et al., 2019, ApJ, 882, 107
Saftly W., Baes M., Camps P., 2014, A&A, 561, A77
Schinnerer E. et al., 2016, ApJ, 833, 112
Schulz S., Popping G., Pillepich A., Nelson D., Vogelsberger M., Marinacci F., Hernquist L., 2020, MNRAS, 497, 4773
Scoville N. et al., 2013, ApJS, 206, 3
Scoville N. et al., 2016, ApJ, 820, 83
Shapley A. E., Cullen F., Dunlop J. S., McLure R. J., Kriek M., Reddy N. A., Sanders R. L., 2020, ApJ, 903, L16
Simpson J. M. et al., 2015, ApJ, 799, 81
Spilker J. S., Bezanson R., Weiner B. J., Whitaker K. E., Williams C. C., 2019, ApJ, 883, 81
Springel V., 2010, MNRAS, 401, 791
Springel V. et al., 2018, MNRAS, 475, 676
Stach S. M. et al., 2019, MNRAS, 487, 4648
Tadaki K.-i. et al., 2017, ApJ, 834, 135
Tadaki K.-i. et al., 2020, ApJ, 901, 74
Torrey P., Vogelsberger M., Genel S., Sijacki D., Springel V., Hernquist L., 2014, MNRAS, 438, 1985
van der Wel A. et al., 2014, ApJ, 788, 28
Van Der Walt S., Colbert S. C., Varoquaux G., 2011, Comput. Sci. Eng., 13, 22
Virtanen P. et al., 2020, Nat. Methods, 17, 261
Vogelsberger M., Genel S., Sijacki D., Torrey P., Springel V., Hernquist L., 2013, MNRAS, 436, 3031
Vogelsberger M. et al., 2020, MNRAS, 492, 5167
Waskom M. et al., 2017, mwaskom/seaborn: v0.8.1. Zenodo. Available at: https://doi.org/10.5281/zenodo.883859
Weinberger R. et al., 2017, MNRAS, 465, 3291
Weingartner J. C., Draine B. T., 2001, ApJ, 548, 296
Whitaker K. E. et al., 2014, ApJ, 795, 104
Whitaker K. E., Pope A., Cybulski R., Casey C. M., Popping G., Yun M. S., 2017, ApJ, 850, 208
Wiseman P., Schady P., Bolmer J., Krühler T., Yates R. M., Greiner J., Fynbo J. P. U., 2017, A&A, 599, A24

APPENDIX A: DEPENDENCE OF THE 1.6 AND 850 μM HALF-LIGHT RADIUS ON THE DUST-TO-METAL RATIO

Our fiducial model adopts a dust-to-metal mass ratio (DTM) that varies as a function of metallicity, with DTM increasing for increasing metallicity, up to a value of 0.32 at a metallicity of 0.4 times solar. This is motivated by observations of dust and CO (and H I) emission in local (and a handful of $z \sim 2$) galaxies (Rémy-Ruyer et al. 2014; De Vis et al. 2019; Shapley et al. 2020, see fig. 1 in Lagos et al. 2019) and high-redshift damped Lyman-alpha and gamma-ray absorbers (e.g. Péroux & Howk 2020, Popping & Péroux, in preparation). Simulations that track the production and destruction of dust have also found the DTM to vary with galaxy properties (e.g. McKinnon, Torrey & Vogelsberger 2016; Popping et al. 2017b; Li et al. 2019). Other simulations found that they require a variable DTM in order to reproduce the UV luminosity of low-mass high-redshift galaxies (Lagos et al. 2019; Vogelsberger et al. 2020). This assumption is different from the classical one of a constant DTM of ∼0.3 often adopted in simulation-based works (see for example Cochrane et al. 2019; Liang et al. 2020; Schulz et al. 2020; Millard et al. 2021).

To estimate the importance of the choice of DTM on our results, we reran the radiative transfer code SKIRT on all the modelled galaxies assuming a constant and universal DTM of 0.3. In Fig. A1, we show the ratio between the 850 and 1.6 μm half-light radius as a function of the mass-weighted gas-phase metallicity when adopting the metallicity-dependent DTM and a fixed DTM of 0.3. Focusing first on 850 μm, we find that this ratio is roughly unity for galaxies with a gas-phase metallicity of 0.75 $Z_{\odot}$ and higher. At lower metallicities the ratio is lower, approximately 0.9 at 0.5 $Z_{\odot}$ and down to 0.8 at even lower metallicities. At 1.6 μm, we find that the ratio is approximately 1.1, independent of the gas-phase metallicity of the galaxies.

In summary, when adopting a fixed DTM of 0.3 the model predicts more extended 850 μm emission and more compact 1.6 μm emission, all typically within 10–20 per cent from our fiducial model. These results suggest that our conclusions are qualitatively robust against expected changes in the DTM. In fact, we have checked that the claims and quantitative statements about the 850 to 1.6 μm size ratios of Fig. 4, top-right panel, remain essentially unchanged to better than the 10 per cent level.

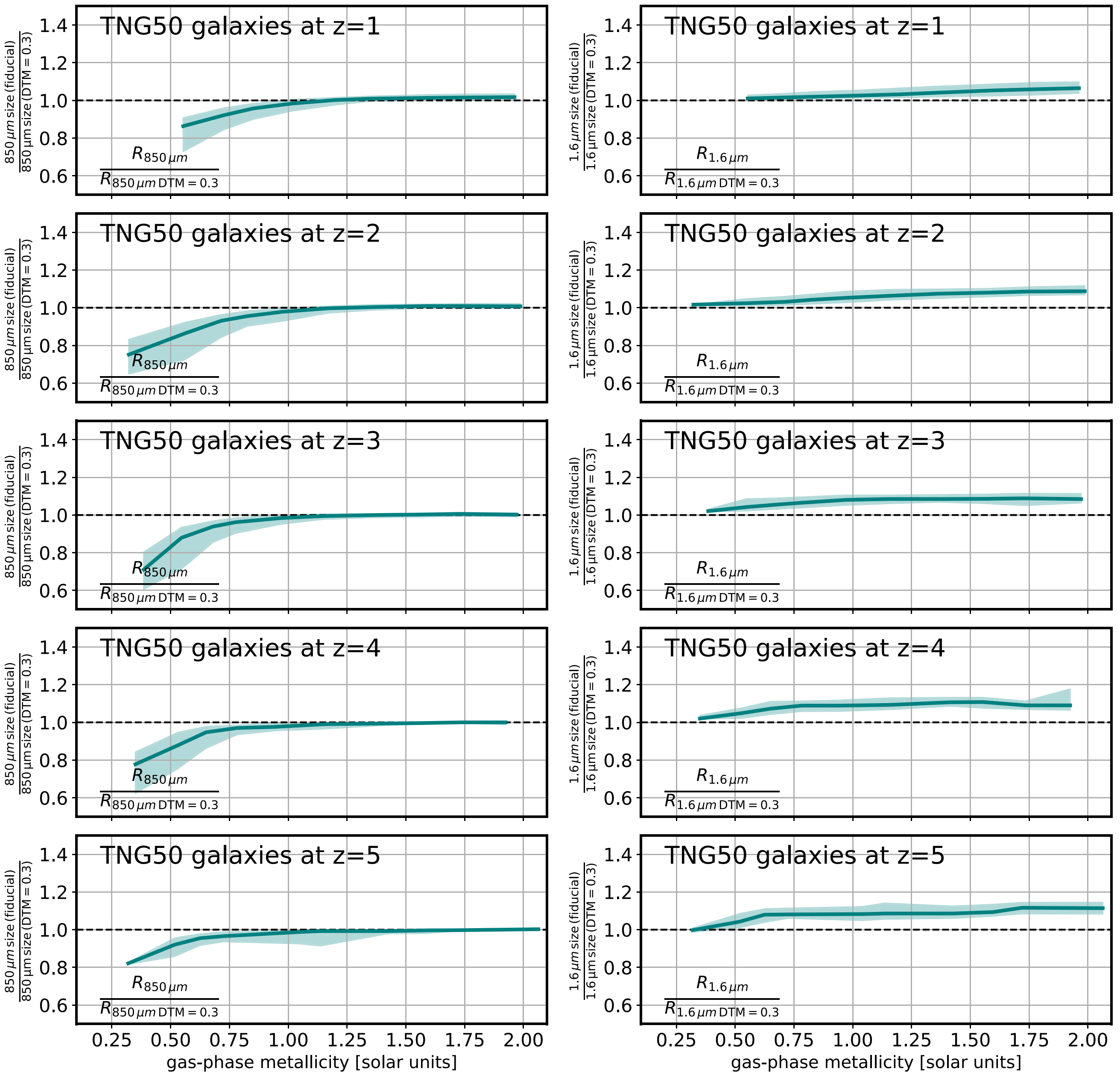

Figure A1. Left column: The ratio between the 850 μm half-light radius of the TNG50 + SKIRT model galaxies when adopting our fiducial metallicity-dependent dust-to-metal mass ratio (DTM) and the half-light radius obtained when adopting a fixed DTM of 0.3, as a function of the mass-weighted gas-phase metallicity of the galaxies. Right column: The same as the left column but for the 1.6 μm half-light radius. The rows indicate different redshifts. When adopting a fixed DTM of 0.3 the model predicts more extended 850 μm emission and more compact 1.6 μm emission compared to our fiducial choice for the DTM. Differences are all within 10–20 per cent from our fiducial model.

This paper has been typeset from a TEX/LATEX file prepared by the author.